



Article

Experimental and Numerical Analysis of a Novel Cycloid-Type Rotor versus S-Type Rotor for Vertical-Axis Wind Turbine

José Eli Eduardo González-Durán ^{1,†}, Juan Manuel Olivares-Ramírez ^{2,*}, María Angélica Luján-Vega ², Juan Emigdio Soto-Osornio ³, Juan Manuel García-Guendulain ¹ and Juvenal Rodríguez-Resendiz ^{4,†}

¹ Automotive Engineering Department, Universidad Politécnica de Querétaro, El Marques 76240, Querétaro, Mexico; eduardo.gonzalez@upq.edu.mx (J.E.E.G.-D.); manuel.garcia@upq.edu.mx (J.M.G.-G.)

² Renewable Energy Department, Universidad Tecnológica de San Juan del Río, San Juan del Río 76800, Querétaro, Mexico; alujanv@utsjr.edu.mx

³ Electronics Department, Tecnológico Nacional de México Campus San Jun del Rio, San Juan del Río 76800, Querétaro, Mexico; emigdio.so@sjuanrio.tecnm.mx

⁴ Facultad de Ingeniería, Universidad Autónoma de Querétaro, Santiago de Querétaro 76010, Querétaro, Mexico; juvenal@uaq.edu.mx

* Correspondence: jmolivar01@yahoo.com

† These authors contributed equally to this work.

Abstract: The performance of a new vertical-axis wind turbine rotor based on the mathematical equation of the cycloid is analyzed and compared through simulation and experimental testing against a semicircular or S-type rotor, which is widely used. The study examines three cases: equalizing the diameter, chord length and the area under the curve. Computational Fluid Dynamics (CFD) was used to simulate these cases and evaluate moment, angular velocity and power. Experimental validation was carried out in a wind tunnel that was designed and optimized with the support of CFD. The rotors for all three cases were 3D printed in resin to analyze their experimental performance as a function of wind speed. The moment and Maximum Power Point (MPP) were determined in each case. The simulation results indicate that the cycloid-type rotor outperforms the semicircular or S-type rotor by 15%. Additionally, experimental evidence confirms that the cycloid-type rotor performs better in all three cases. In the MPP analysis, the cycloid-type rotor achieved an efficiency of 10.8% which was 38% better than the S-type rotor.

Keywords: 3D printed; CFD; cycloid; maximum power point; rotor; vertical-axis wind turbine; VAWT; wind turbine



Citation: González-Durán, J.E.E.; Olivares-Ramírez, J.M.; Luján-Vega, M.A.; Soto-Osornio, J.E.; García-Guendulain, J.M.; Rodríguez-Resendiz, J. Experimental and Numerical Analysis of a Novel Cycloid-Type Rotor versus S-Type Rotor for Vertical-Axis Wind Turbine. *Technologies* **2024**, *12*, 54. <https://doi.org/10.3390/technologies12040054>

Academic Editor: Miklas Scholz

Received: 28 February 2024

Revised: 13 April 2024

Accepted: 15 April 2024

Published: 17 April 2024



Copyright: © 2024 by the authors. Licensee MDPI, Basel, Switzerland. This article is an open access article distributed under the terms and conditions of the Creative Commons Attribution (CC BY) license (<https://creativecommons.org/licenses/by/4.0/>).

1. Introduction

Climate change has significantly affected Earth's meteorological conditions, leading to consequences such as natural disasters and impacts on both humans and the environment. Among the efforts to mitigate the consequences of climate change there are various scientific contributions and technological developments, such as photovoltaic power generation [1,2], organic solar cells [3] and fuel cells [4,5]. In the field of wind energy, there are significant developments and studies such as large-capacity horizontal wind turbines for energy generation [6]. Two main types of Vertical-Axis Wind Turbines (VAWTs) are present in the literature, namely Savonius and Darrieus. The primary difference between them lies in their operation: Savonius turbines (S-type) operate based on drag-driven principles, while Darrieus turbines focus on lift-driven principles, which means they have high aerodynamic efficiency, reaching the theoretical Betz Limit. Research into studying, developing and improving the performance of different VAWTs can be found in the literature through computational fluid dynamics (CFD) and experimental methods.

For example, research related to the use of CFD includes studies by Day et al. [7], Zhang et al. [8] and Ye et al. [9]. They investigated the influence of two parameters on

the performance of a VAWT using CFD: the airfoil's maximum camber and its position along the chord. Regarding the methodology, some studies have focused on calculating the uncertainties associated with the use of CFD, evaluating the wing section of the NREL S826 airfoil and conducting experimental validation. Celik et al. [10] utilized CFD to examine how the moment of inertia and the number of blades influence both the aerodynamic characteristics and the power output of an H-type VAWT. Ghareghani et al. [11] and Li et al. [12] performed detailed numerical evaluations of the aerodynamic performance of a VAWT, varying the helix angles within the range of 60° to 120° . Ali et al. [13] utilized dynamic 2D simulations with CFD to explore how the airfoil shape and blade pitching impact VAWT. Their results revealed that the pitch angles of the blade set in an out-offset manner demonstrated superior performance when compared to those set in an in-offset manner. Similarly Jiang et al. [14] conducted a 2D analysis using CFD to examine the variation in blade aerodynamic torque based on the blade angle of attack (AoA). Ghoneam et al. [15] carried out modeling and optimization for the dynamic performance of composite blades in VAWTs using simulations in commercial software. Wilberforce and Alaswad's [16] development of augmented turbine blades resulted in a 1.35-fold increase in power output compared to an open rotor. Research by Singh et al. [17] involved an examination of the efficiency of the power production of H-Darrieus vertical-axis wind turbines (HDWTs) with three blades with varying aspect ratios. This was achieved by altering the turbine diameter and calculating the moment and power coefficient values within a tip speed ratio (TSR) range of 1.5 to 3.5. The findings indicated that HDWT with a smaller aspect ratio (AR) of 0.44 outperformed other test conditions, achieving a higher power coefficient of 0.294 in TSR 2.5. The research of Huang et al. [18] introduces an innovative variable solidity Darrieus-type vertical-axis wind turbine (D-VAWT) to address the issue of self-starting and enhancing aerodynamic performance. The results of the study reveal that the solidity (σ) and the moment of inertia (J_z) significantly impact the self-starting capacity. Consequently, the maximum power output of a single D-VAWT increased from 53.42 W to 100.39 W, resulting in a remarkable 188% power increase. The study of Farzadi and Bazargan [19] indicates that the substitution of straight blades with J-type blades results in a 26.9% torque increase at a wind speed of 10 m/s and a 37.6% torque increase at a wind speed of 5 m/s. In the investigation of Tong et al. [20], the impact of airflow at the tip of the blade on the aerodynamic properties of SB-VAWTs is investigated through numerical simulations. The analysis encompasses a diverse set of 84 models, with variations in parameters such as rotor diameter, blade chord length, tip speed ratio, blade aspect ratios (AR) and airfoil types. This study is expected to provide a valuable resource for the design of SB-VAWTs and establish a foundation for subsequent investigations into optimizing blade tips. The paper of Li et al. [21] suggests an innovative approach to situating VAWT on the exteriors of existing buildings, using the buildings themselves as support structures. Notably, when the diameter of the built-in structure is reduced to 50% of the rotor diameter, the resulting power coefficient (C_p) loss is less than 20% and this relationship is not linear within that 50% range. The study of Shubham et al. [22] involves a comparison of two analytical aerodynamic techniques: the low-fidelity Double Multiple Streamtube method and the mid-fidelity Lifting Line Free Vortex Wake method. Tong et al.'s [23] findings in this investigation have established the importance of a dimensionless parameter called the RCC, which represents the ratio of the airfoil chord length to the rotor circumference. RCC is revealed to be a crucial factor in the design of SB-VAWTs. The objective of Xu et al. [24] in their article is to improve the efficiency of Savonius VAWT through the application of flow control techniques, specifically employing a relatively novel approach known as plasma excitation flow control. To achieve this, they utilized the User-Defined Function (UDF) in ANSYS Fluent to apply plasma excitation sources to the blades of the Savonius VAWT.

In the literature, there are studies related to the experimental aspects of VAWT; for example, Hohman et al. [25], Kuang et al. [26] and Vergaerde et al. [27] have conducted studies using High-Resolution Particle Image Velocimetry to analyze the effects of blade sweep on VAWTs. Additionally, research has explored the impact of rotor solidity on the power

performance and aerodynamics of VAWTs, employing high-fidelity Improved Delayed Detached-Eddy Simulations. As another example, Thomai et al. [28] conducted an experimental and numerical investigation of a new development of a helical Bach-type VAWT, which features a modified form of a Savonius model with circular and straight portions in the blade profile and found superior performance compared to the helical Savonius model. Some other authors have conducted studies on sinusoidal profiles, deflectors and various configurations; for example, in the case of [29–31] in the field of sinusoidal profiles, five types were characterized, including leading-edge protuberances with three different wavelengths and amplitudes. These were studied on an H-type Darrieus VAWT using unsteady Reynolds-averaged-Navier–Stokes (URANS) and implicit large-eddy simulation (ILES) methods. Lastly, in different configurations, arrangements of a set of VAWT were constructed on a single shaft to improve the average power output. Zheng et al. [32] developed a floating VAWT concept and tested it under wind and wave interactions. Shah et al. [33] found that the variable pitch design significantly increased power production compared to the fixed pitch design. Ghoneam et al. [34] present a dynamic analysis of Optimized Savonius VAWT Composite Blades, enhancing cleanliness, silent operation, startup under low wind speeds, independence from wind directions, adaptability and ease of manufacturing. The dynamic characteristics, including frequency, mode shape and damping factor, were extensively investigated using a fast Fourier transform (FFT) analyzer. Su et al. [35] used a numerical model and its experimental validation to investigate the effect of the swept blade employed in a VAWT on improving its aerodynamic performance.

Several other works reported in the literature combine numerical simulation with experimental tests in well-conditioned wind tunnels, designed for specific purposes, such as Roy et al. [36], who realized simulations on various airfoils of NACA 4-series, 5-series and Selig profiles at different chord Reynolds numbers of 60,000, 100,000 and 140,000. Investigations by Seralathan et al. [37] revealed that, out of the three deflector configurations, the front deflector contributed to a beneficial local airflow around the blade, leading to enhanced performance. Su et al. [38] evaluated this performance in comparison to different setups involving two VAWTs and determined that a separation of 1.5 times the rotor diameter was necessary to mitigate the turbulence interaction. Tanzawa et al. [39] studied, through computer simulation and wind tunnel testing, the characteristics of wind direction on a VAWT developed by the authors using a mechanism inspired by a bird's wing.

In the literature, there are also studies on aerodynamic performance and its effects on the development of VAWTs, as in the case of Rahman et al. [40], who studied Helical Shape VAWT Models with different blade numbers, employing both wind tunnel experiments and CFD. Naik et al. [41] analyzed the effect of a J-shaped aerodynamic profile on the performance of the straight-bladed Darrieus vertical-axis wind turbine. Sarkar et al. [42] investigated slotted Bladed Darrieus VAWT through numerical analysis and found that slotted airfoils exhibited an improved lift coefficient and power coefficient compared to airfoils without slots. Zilberman et al. [43] tested 30 VAWT models derived from parametric variations of 5 basic models while maintaining the same aspect ratio but altering the number of bucket phases, orientation angles and the gaps between vanes. Ultimately, ref. [44] employed CFD to gain insights into the forces and moment behaviors of the optimized turbine. In the study of Liu et al. [45], the authors investigated the type of VAWT equipped with four helical blades using Detached Eddy Simulation (DES), which was experimentally validated and compared with results obtained in a transient state. Furthermore, a numerical analysis conducted by Mohammed et al. [46] discovered that a fixed pitch of -2.5 degrees could significantly improve the performance of the VAWT. Additionally, they found that the negative value of the average power coefficient was associated with the best starting capability and a moderate peak power coefficient. A numerical investigation was performed by Yan et al. [47] to analyze how the addition of a Gurney flap (GF) affects the aerodynamic performance of the NACA 00 airfoil and a three-blade rotor used in an H-type Darrieus wind turbine. Li et al. [48] explored the assessment of the aerodynamic efficiency and vortex behavior of a straight-blade VAWT along the spanwise direction.

Among the published works, there are also developments of VAWT for specific applications or some attachments that can enhance their performance, as in the case of [49], which proposes a hybrid Savonius and Darrieus system with a mechanism that can operate them separately or together. Korprasertsak and Leephakpreeda [50] developed a concentrator and amplifier type to achieve optimal airflow over the VAWT. Vlasveld et al. [51] simulated the coupled dynamics of a 6 MW VAWT with active blade pitch control, supported by a GustoMSC Tri-Floater semi-submersible floater, using specialized software. Mishra et al. [52] performed an experimental and numerical investigation, employing CFD, to assess and contrast the performance of Darrieus turbines when utilizing different wingtip devices. Wang and Zhuang [53] carried out a numerical analysis to explore how a VAWT would perform when equipped with straight blades featuring serrated leading-edge configurations in a traditional H-type VAWT design, aiming to control dynamic flow separation.

Chen et al. [54] develop research related to the behavior of groups of Savonius turbines, which operate under the same rotation speed, optimizing the power coefficient 1.425 plus that of the groups of an isolated turbine, using the Taguchi method. In the area of hydrokinetic turbines, Nag and Sarkar [55] analyzed Savonius-type helical systems; an improvement is obtained when the separation distance is four times the turbine diameter and they are distributed in a triangular formation, the optimal way to distribute the turbines was staggered.

Various applications of the cycloid have been reported in the literature, mainly focusing on the development and improvement of transmissions or mechanisms. However, there is a notable absence of references to applications involving VAWTs. For example, applications within the field of mechanics [56] report an experimental and theoretical approach to assess the efficiency of a cycloidal drive reducer. Li et al. [57] suggest an analytical framework for a cycloid speed reducer, using unloaded tooth engagement and load distribution analyses as its foundation. Zhu et al. [58] investigated a cycloid gear drive and its performance in lubrication, employing a numerical finite line starved-elastohydrodynamic lubrication model. Sensinger [59] incorporates modification factors for various transmissions that fall under this category, including cycloids and harmonic drives, validates that the models are in line with experimental findings and demonstrates that within this subgroup of transmissions, efficiency becomes a function of the torque ratio. Rashidi et al. [60] develop an efficient self-tuning vibration absorber capable of adapting its performance to the excitation frequency. Another application within the field of mechanics is provided by Choi et al. [61] suggesting the design of a rotor for an internal gear pump employing cycloid and circular-arc curves. To demonstrate performance improvement, they analyzed the internal fluid flow through CFD using commercial software. Hong Kim et al. [62] analyzed a cycloid drive, taking into account finite bearing and Hertz contact stiffness. Another study by Sensinger [63] presents the optimized design of cycloid drives, known for their compact and efficient speed-reduction capabilities. In their precision transmission work, ref. [64] demonstrated that efficiency is improved even though torque decreases in cycloid gear trains. Tutulan et al. [65] conducted a contact stress analysis of the modified cycloid helical gear, which was designed with a non-involute tooth profile derived from the cycloid tooth profile. This gear exhibits greater surface durability compared to the involute helical gear. Zhou [66] created a novel cycloid drive with ceramic balls as its gear teeth. Li et al. [67] patented a double crank plate-type cycloid drive characterized by its high load capacity and efficiency. Blanche and Yang [68] find that the cycloid drive, when compared to a conventional gear mechanism, offers exceptionally high efficiency and compact size, making it an attractive choice for applications with limited space. Pollitt [69] lists various applications of the cycloid in machine design, such as the multi-lobed epicycloid. Mao et al. [70] describe an innovative cycloidal planetary reducer that employs an internal meshing principle, departing from the traditional RV reducer's external meshing between the cycloidal wheel and pins, specifically in the two-stage cycloidal planetary design.

Finally, after reviewing and presenting the state of the art, it was found that the most relevant application of the cycloid related to airflow is by Ohya et al. [71]; they have

designed a wind turbine system comprising a diffuser shroud with a wide-ring flange at its outer edge, housing a wind turbine within. Liu et al. [72] presented an effective optimization technique for shaping the axis-symmetric wind lens to enhance wind velocity and reduce drag force. Finally, Zimmer and Gagnon [73] conducted the study on the performance of a cycloidal rotor in hover at different Reynolds numbers; however, they refer to the cycloidal rotor (or cyclorotor) as a rotating-wing system and not the development of a VAWT. Therefore, in the literature, there is still no reported study on the performance of the cycloid in the development of a VAWT.

The investigations described above address the study, improvement, analysis and re-design of VAWTs based on conventional models. However, none of them have mentioned or explored a novel geometry such as the cycloid to be employed in the rotor of a VAWT, as presented in this research. The proposal entails a new blade design for the development of a VAWT, grounded in the parametric equations of the cycloid.

In the present work, a numerical and experimental analysis is presented using CFD to assess the performance of a new cycloid-type rotor (R_C) compared to an S-type rotor for the development of a VAWT.

2. Methods

This section is divided into four stages: the methods and fundamentals used to carry out the CFD simulation of the three proposed cases and the cycloid. The issues for the development of the wind tunnel include CFD simulation and the materials used for construction. In the final stage, the construction of the system and the rotors printed using additive manufacturing are described under the two experimental tests conducted to calculate them: power, determination of the moment and maximum power point (MPP).

Figure 1 displays the diagram methodology used in this investigation. First of all, a new blade design is proposed based on the parametric equations of a cycloid against an S-type rotor. Then, cases with different variants are defined, including the same arc for an S-type rotor case I (S_{C1}), the same chord for an S-type rotor case II (S_{C2}) and the same area under the curve for an S-type rotor case III (S_{C3}), compared to the unique Cycloid-type rotor (R_C). The geometries of the cases were evaluated using CFD with ANSYS®. In this stage, the root-mean-square (RMS) power values were analyzed to determine if the R_C was higher than any case for S-type rotors. If the final stage yields positive results, we proceed to design a wind tunnel to assess the performance of the cases and R_C . The following step involves designing the wind tunnel based on two criteria. If both criteria are met, the wind tunnel will be used to characterize the 3D printed rotors that were evaluated in simulation with established airflow fields. The experimental moment will then be determined, followed by the evaluation of the maximum power point (MPP). If the experimental evaluations show that the performance of the R_C is higher than that of the S-type cases, the study will be considered successful.

2.1. Geometries

We calculate an arc of a cycloid, which is generated by a point belonging to a generating circle, rolling along a straight guideline (for the “ x ” axis), without the circle slipping. The parametric equations that govern the cycloid [74] are:

$$x = r(\theta - \sin \theta) \quad (1)$$

$$y = r(1 - \cos \theta) \quad (2)$$

where x is the coordinate on the abscissa axis, R is the radius of the generating circle, θ is the angle in radians, which is measured between the vertical segment passing through the center of the generating circle, perpendicular to the abscissa axis (x) and the radius (r). Finally, y is the coordinate on the ordinate axis.

For the S-type turbine, the geometry was defined using a circular arc [50] and the parametric equations are as follows:

$$x = r \cos \theta \quad (3)$$

$$y = r \sin \theta \quad (4)$$

The performance assessment of different geometrical blades for VAWT development was compared using three cases and a cycloidal-type rotor (R_C) as shown in Figure 2.

1. Case I (S_{C1}): the diameter (4.5 cm) of the S-type rotor (S_{C1}) with circular geometry is equal to 4.5 cm of the R_C directrix.
2. Case II (S_{C2}): the chord (5.7 cm) of the S-type rotor (S_{C2}) with circular geometry is equal to the chord (5.7 cm) of the arc of the (R_C) geometry.
3. Case III (S_{C3}): the area under the curve (4.8 cm²) of the S-type rotor (S_{C3}) with circular geometry is equal to the area under the curve (4.8 cm²) of the arc of the (R_C) geometry.

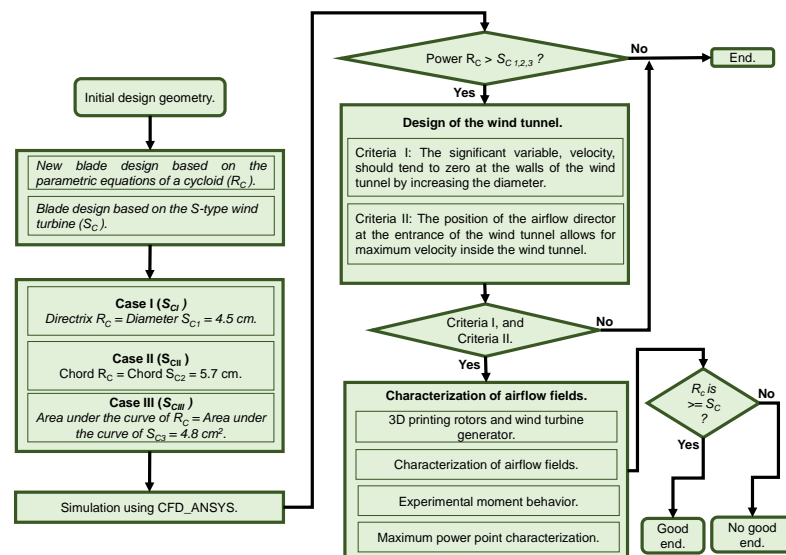


Figure 1. The methodology diagram followed in this investigation.

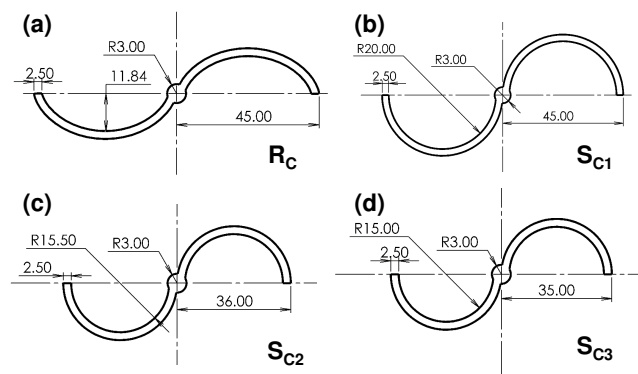


Figure 2. Geometrical description of blades for the 3 proposed cases. (a) The Cycloid-type rotor (R_C); (b) S-type rotor for Case I, where the diameter (45 mm) of S_{C1} is equal to the directrix of R_C ; (c) S-type rotor for Case II, where the chord (57 mm) of S_{C2} is equal to arc of R_C ; (d) S-type rotor for Case III, where the area under the curve (480 mm²) of S_{C3} is equal to the area under the curve of R_C . Dimensional units in mm. All rotors have a height of 120 mm.

2.2. CFD

Within this section, the main stages of simulation through CFD are specified, which include the modeling of geometries, meshing and boundary conditions established for all the cases.

2.2.1. Modeling of Geometries

The computational domain was constructed with the dimensions described in Figure 2, similar to the studies by Sobczak [75], Mohamed et al. [76] and Sobczak et al. [77]. This ensures that the comparisons between different rotor configurations are not affected. As one can see in Figure 3, the fluid domain was divided into two regions. The internal domain of the diameter $1.5D$ including rotors was surrounded by the external one with an interface. The total length of the domain was $60D$ in the flow direction, with the turbine axis located $20D$ from its inlet and in the middle of the domain height, which was set to $40D$; the real domain dimensions do not correspond to the scale.

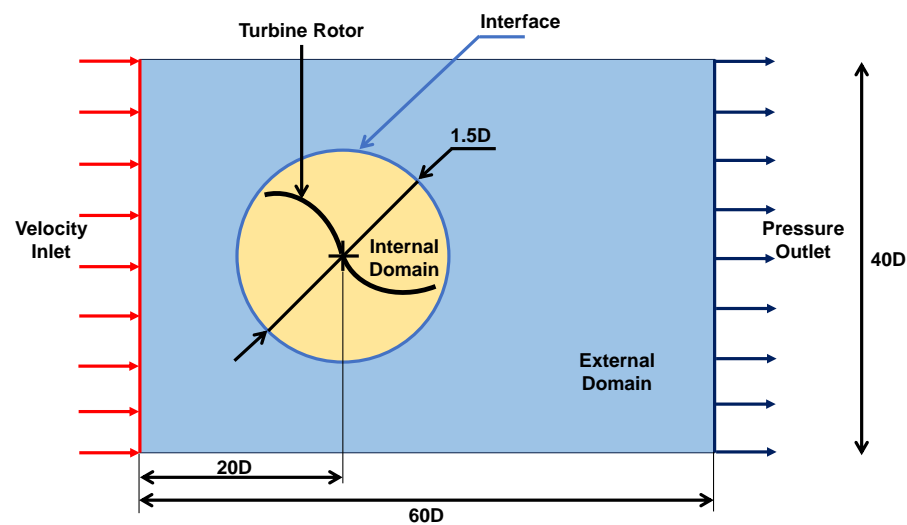


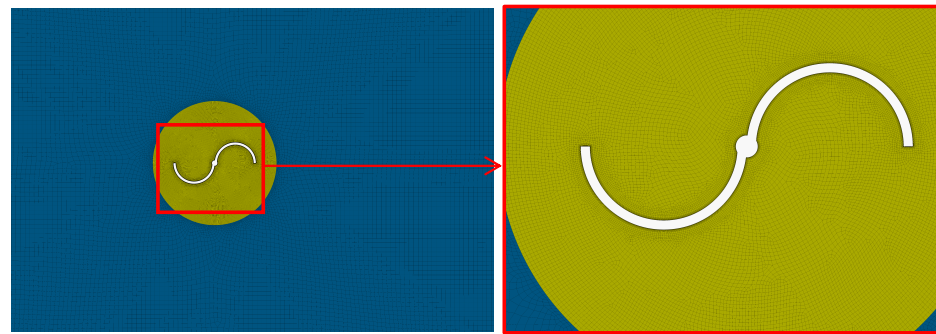
Figure 3. Computational domain scheme (dimensions do not correspond to the scale).

2.2.2. Mesh

The computational mesh was generated in ANSYS® using quadratics elements, with a refinement of 0.5 mm in the rotors and 12 layers of inflation with a growth rate of 1.2, elements of 1 mm size in the internal domain and the external domain was meshed with a refinement of 5 mm. Refinements were applied around the interface with the internal domain (Figure 4). Richardson's extrapolation was used to verify the dependence on mesh size, as was done by Sobczak et al. [78] and Aramendia et al. [77]. The same task was solved on three different grids with a mesh refinement ratio of 2 for S_{C1} and 1.95 for R_C . The numbers of control volumes of the grids and the RMS power values obtained for them are presented in Table 1. According to the Richardson's extrapolation procedure described by Kacprzak and Sobczak [79], Sakri et al. [80] and Celik et al. [81], the extrapolated value (RE), the apparent order p , the ratio of error R and the fine-grid convergence index ($FGCI$) were determined. The R value in both cases indicates a monotonic convergence. Only a slight variation in the average RMS power was observed for R_C (3.5%). The uncertainty due to discretization was determined for the RMS power values based on Richardson's extrapolation procedure described by Celik et al. [81]; in accordance with Table 1, the highest numerical uncertainty in the fine grid solution for the R_C mesh was low, i.e., 2.25%. Because it is less than 5%, it was decided to use it in this work.

Table 1. Mesh size dependence study.

	Mesh			Richardson's Extrapolation			
	Coarse	Medium	Fine	RE	p	R	$FGCI$
R_C	248,570 0.3235	564,877 0.3324	849,869 0.3384	0.3508	0.61	0.67	2.25%
S_C	204,202 0.2753	482,799 0.2929	805,162 0.2941	0.2942	3.87	0.07	0.16%

**Figure 4.** Computational mesh in the external and internal domains with details of its refinement in the blade vicinity.

2.2.3. Boundary Conditions

The numerical analysis was conducted in a transient 2D planar model, a pressure-based solver and k-epsilon turbulence model. The Dynamic Mesh model, specifically Six DOF with smoothing and remeshing, was employed. Simulation variables and the boundary conditions defined for the CFD analysis are described in Table 2 for both the R_C and the S_{C1} . The simulations were carried out for the tip speed ratio $TSR = 0.8$, for which Savonius rotors reach the maximal value of the power coefficient C_p . For this TSR , the angular velocity of the turbine was 44.44 rad/s . Thus, the selected timestep of 0.001 s corresponded to a revolution of the rotor by approximately 2.54° , resulting in 142 steps per one revolution, which is sufficiently low as far as the time discretization is concerned. The step size was also verified through the residuals jumping at the beginning of each time step and then falling at least two to three orders of magnitude. Also, the relative convergence criteria are achieved before reaching the maximum iteration limit (60) for each time step, indicating the limit does not need to be increased.

Table 2. Boundary conditions defined for the simulation of the R_C and S_{C1} .

Variable	S_{C1}	R_C
v inlet (m/s)		2.5
Pressure outlet (Pa)		0
Mass (kg)	0.042	0.034
Moment of inertia ($\text{kg}\cdot\text{m}^2$)	3.83×10^{-5}	2.58×10^{-5}
Pressure–velocity coupling		Simple
Gradients		Least squares cell based
Pressure		Second order
Moment		Second order upwind
Time step size		0.001
Number of time steps		3000
Max. iterations		60

In the single-variable solution, for the convergence value a residual quantity of 1.0×10^{-4} was considered for the continuity equation and 1.0×10^{-6} for the other residuals.

The variables used to quantify the rotor's performance were the moment generated by the rotor in Newton meters (N·m) and the angular velocity in radians per second (rad/s). The maximum velocity at the rotor's radius was considered for the angular velocity. Once the results for the S-type rotor and the new R_C rotor were obtained, experimental behavior was evaluated.

2.3. Design of the Wind Tunnel

The design is based on the conditions present in San Juan del Río, Querétaro, Mexico (latitude 20.3915, longitude -99.9814 , $20^{\circ}23'29''$ N, $99^{\circ}58'53''$ W), considering the compass rose for this location. Minimum wind speeds of 0 m/s, maximum speeds of 11.03 m/s and an average of 2.5 m/s are recorded in [82]. Therefore, the speed considered for the wind tunnel design and simulations was 2.5 m/s.

2.3.1. Velocity Fields

The initial step comprised modeling and optimizing the wind tunnel with ANSYS[®] CFD. A central cylinder was constructed to accommodate the wind turbine, as depicted in Figure 5, with fluid properties. In Figure 5a, the front face, designated as INLET, can be seen with the following dimensions: a length of 15 cm and a diameter of 30 cm. The outlet (Figure 5b) has the same dimensions as the inlet and the back face was designated OUTLET. The central cylinder of the wind tunnel (Figure 5g) has a length of 100 cm and a diameter of 75 cm. In the middle of the wind tunnel, a cube (Figure 5c) with sides of 12 cm was constructed to simulate the control volume where the wind turbine will be housed.

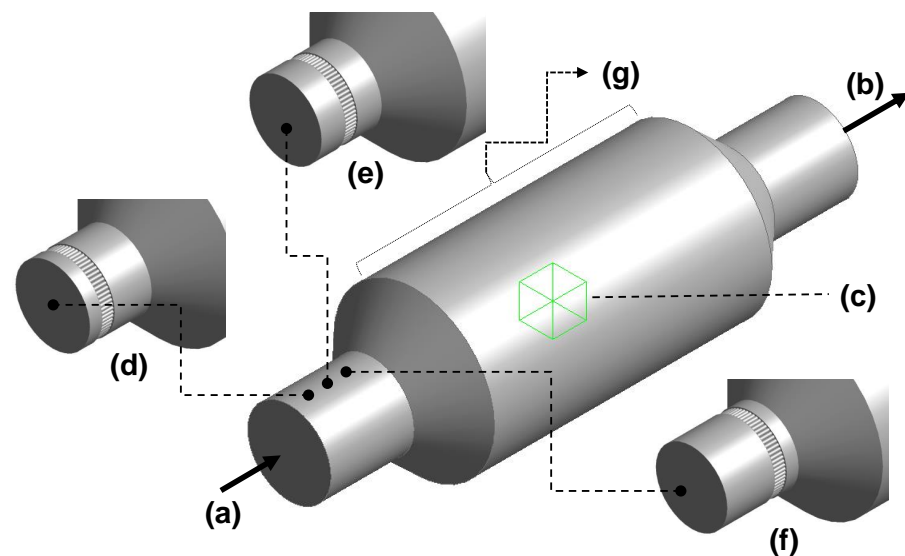


Figure 5. Solid model of the wind tunnel; (a) Selected surface for the air flow inlet, (b) Selected surface for the air outlet, (c) Central volume to house the wind turbine, (d) Flow director at the entrance, (e) Flow director in the middle, (f) Flow director at the end and (g) Central cylinder.

The meshing is carried out with an element size of 1 cm, 170,963 nodes and 906,480 elements. Simulations are performed for 4 cases: the first one considering an inlet velocity of 1 m/s, the second with an inlet velocity of 4 m/s, the third with a velocity of 8 m/s and finally the fourth with 12 m/s. The wind tunnel will perform better when it reaches the following criterion.

Criterion I: The significant variable, velocity, should tend to zero at the walls of the wind tunnel by increasing the diameter.

2.3.2. Airflow Director

As the air comes from a fan, the flow fields are torsional, exhibiting turbulence. It is necessary to have flow fields that exhibit coplanar vector profiles. A flow field director was inserted to achieve this, as seen in Figure 5d–f. Simulations were conducted for the three positions of the flow director: 5 cm at the entrance (Figure 5d), in the middle (Figure 5e) and 5 cm at the end (Figure 5f). It is considered that the best performance will be achieved when it reaches the following criterion.

Criterion II: The position of the airflow director at the entrance of the wind tunnel allows the maximum velocity inside the wind tunnel.

Finally, the materials used for the 1:1 scale construction were the following: anodized flat profile of 3.2×0.2 cm and 300 cm in length, the structure was covered with 12-gauge clear plastic and the flow directors were constructed using 1.27 cm diameter, 2.54 cm long white CPVC pipe, Amanco®.

2.4. Construction and Characterization of the 3D Printed Rotors

The following section outlines the materials and methods used to conduct experimental tests on the previously described cases and the R_C inside the wind tunnel, as well as power determination.

2.4.1. 3D Printing Rotors and Wind Turbine

Inside the lower base of the wind turbine shown in Figure 6a, it was constructed using 10.16 cm diameter tubing made of Nylon-Acetal-UHMW-Teflon-HDPE, with a height of 30 cm. It contains a 3V–5V DC motor with a permanent magnet, a Ky-003 Magnetic Hall Effect Sensor module together with a Laser Non-Contact Tachometer to quantify RPM and a Rantec Rs-one card for data acquisition and processing. The 12 cm high rotors for the R_C geometry (Figure 6b) and S_{C1} , S_{C2} and S_{C3} (Figure 6c–e) were 3D printed, using the Creality Halot Max high-resolution and precision equipment. Once printed, the blades are connected to the electric motor using a 0.4 cm diameter and 16 cm long shaft.

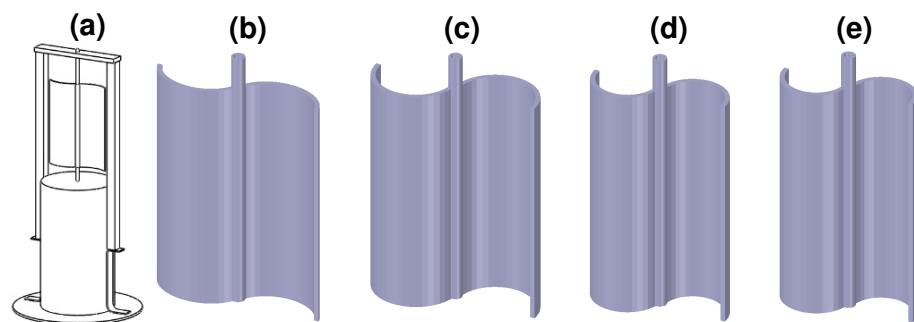


Figure 6. Wind turbine and rotors. (a) Wind turbine, (b) R_C Rotor, (c) Rotor S_{C1} , (d) Rotor S_{C2} and (e) Rotor S_{C3} .

2.4.2. Characterization of Airflow Fields

In the first stage, the airflow is characterized based on RPM by placing the wind turbine inside the tunnel. The wind speed was measured using a UNIT-C LCD digital anemometer model Ut363s and the rotor's RPM was recorded with a General Tools & Instruments LT2234C Laser Non-Contact Tachometer. The objective was to determine the Power Coefficient (C_p), which is defined as:

$$C_p = \frac{\text{Energy by the wind turbine}}{\text{Total energy available in the wind}} \quad (5)$$

The calculation of wind power typically involves using the equation that provides the theoretical wind power for a given swept area by a wind turbine:

$$P = 0.5 \cdot \rho \cdot A \cdot v^3 \cdot C_p \quad (6)$$

where P is the power in watts, 0.5 is a constant which results from the kinetic energy equation, ρ is the air density in kg/m^3 , A is the circular area in m^2 swept by the rotor blades, v is the oncoming wind velocity in m/s and C_p is the power coefficient (efficiency) and it is the percentage of wind power converted into usable energy.

The highest possible extraction of kinetic energy from the wind occurs when the most significant reduction in wind speed is achieved while still ensuring there is enough airflow past the turbine blades. Betz, through his observations and calculations, determined that with an optimal three-bladed design, no more than approximately 59.3% of the incoming wind's kinetic energy can be harnessed. So, in Equation (6), C_p can be replaced with the Betz Limit of 59.3% (0.593) that corresponds to the maximum of the power coefficient. Nevertheless, this presupposes that the wind turbine can extract power without any losses, operating at 100% efficiency. In practice, achieving 100% efficiency in turbines is unattainable, even when they are operating at their maximum speed, owing to the inherent mechanical constraints of their design and operation.

The blade tip speed ratio (TSR) λ is defined as the ratio between the rotor speed and the relative wind speed, as defined by the equation:

$$\lambda = \frac{\omega R}{V_w} \quad (7)$$

where ω is the angular velocity in rad/s , R is the rotor radius and V_w is the wind speed. It is also important to mention that for power generation, TSR is considered greater than 4. Thus, based on the power coefficient C_p , we can relate both variables and determine the behavior of C_p as it changes for any wind turbine.

2.4.3. Experimental Moment Behavior

In the second stage, two BK precision multimeters of model 2707B were used to measure voltage, current and electrical resistance. Additionally, a BK precision power supply model 1672 was used to generate the power supply voltage for the electric motor.

In addition, a fan with three operating options was used: low speed (4 m/s), medium speed (5 m/s) and high speed (6 m/s). Each rotor for S_{C1} , S_{C2} and S_{C3} , as well as the R_C , was coupled to a shaft connected to a brushless, permanent magnet DC electric motor with a nominal operating voltage of 5 V, an operating speed of 16,000 RPM, a maximum current of 1.3 A, operating loads ranging from 0.1×10^{-3} Nm to 0.98×10^{-3} Nm, bidirectional rotation, a shaft diameter of 0.2 cm and length of 0.75 cm, which was used as an electrical generator. Therefore, the procedure involves using the equation:

$$T = k\phi I \quad (8)$$

where T is the torque of the momentum in N·m, the factor $k\phi$ was experimentally determined through tests on the electric generator coupled to each rotor in each case. The slope of the graph of angular velocity vs. induced voltage is represented by factor $k\phi$. The current generated when attempting to brake the rotation of the generator energized with its operating voltage (V_i), using the air from the fan applied to the rotor of each case, which is coupled to the electric generator, is represented by I . This current is generated when the air moves the rotor anchored to the electric generator's shaft.

2.4.4. Maximum Power Point Characterization (MPP)

The third stage involved characterizing the maximum power point. To conduct this test, the fan was activated and resistances of 3.6, 36.66, 44, 55, 73.33, 110, and 220 ohms

were added as loads to the electric generator to determine the MPP. Only the low and high-speed options of the fan were utilized for this test.

3. Results

This section presents and discusses the results obtained from the CFD simulations, wind tunnel design, experimental determination of moment or torque and power values obtained from the characterization of the MPP.

3.1. Simulation with CFD

After conducting the numerical simulation with ANSYS® FLUENT, the data for moment and angular velocity were processed to assess the RMS power values obtained in each case and quantitatively determine the best performance among the evaluated cases. Figure 7 shows the results obtained for R_C and S_{C1} .

The power is calculated based on the torque and angular velocity obtained from the simulations, where the value reached is approximately 338.40 mW for R_C and 294.10 mW for S_{C1} . Those values represent the result of the RMS. The simulation results for velocity (Figure 7c,d) show the highest values in red. The maximum velocities for R_C were 6.61 and 5.87 m/s for S_{C1} . Since the simulation is in a transient state, it allows visualization of the rotor movement, which rotates counterclockwise. This motion induces speeds of up to 6.61 and 5.87 m/s at the bottom of the rotors and speeds approaching 0 m/s at the top, as the wind flow direction opposes the rotor movement. Additionally, in Figure 7c,d, the relative wind speed at a midway point of the boundary layer of the aerodynamic profile is observed to be approximately 4.4 and 3.9 m/s for R_C and S_{C1} rotors, respectively. This implies that the proposed profile can enhance the speed, increasing the TSR. In the pressure profiles of Figure 7a,b, the red zones indicate the highest pressure values. The maximum value for S_{C1} is 6.52 and 6.24 Pa for R_C . In this case, although S_{C1} is higher than R_C , the surface with the red value is higher in R_C than in S_{C1} . Additionally, the negative pressure values are higher in R_C than in S_{C1} . As a result, R_C reaches a higher velocity than S_{C1} and the power values are also higher in R_C . These findings suggest that pressure gradients in the rotor play a significant role in the system's motion.

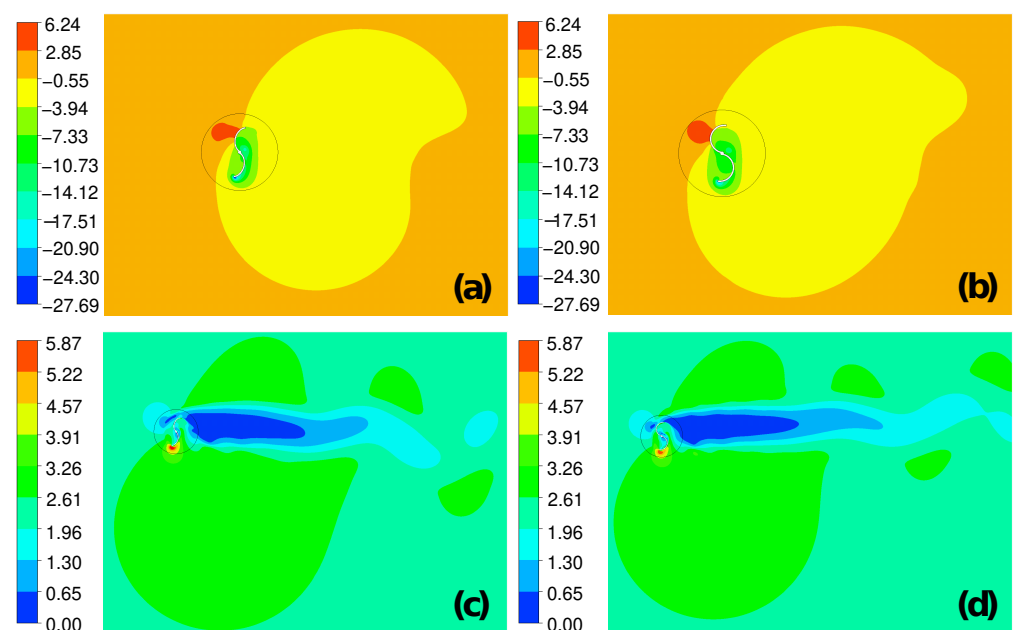


Figure 7. Maximum pressure and velocity fields: (a) pressure contour and (c) velocity contour for R_C . (b) Pressure contour and (d) velocity contour for S_{C1} . Pressure units are Pa and velocity units are m/s.

Power is a fundamental variable in the development of a wind generation system. The simulation results for the four rotors are as follows: 338.4 mW for the R_C rotor, 294.1 mW, 32.9 mW and 29.1 mW, for S_{C1} , S_{C2} and S_{C3} , respectively. The results of the 2D simulation allow for comparison:

- If the diameter of the semicircular geometry for the S_{C1} is equal to the directrix of the R_C , which is 4.5 cm, the power will be 1.15 times greater than that of the S_{C1} . This indicates that the R_C will provide better performance.
- If the chord length of the S_{C2} is equal to the chord length of the arc of the R_C (5.7 cm), the power output of the R_C is 10.44 times greater than that of the S_{C2} .
- If the area (4.8 cm²) under the curve of the S_{C3} rotor is equal to the area (4.8 cm²) under the curve of the arc of the R_C , the power is 11.60 times greater than S_{C3} .

The results reveal that R_C exhibits the highest power value and it is 15% better than S_{C1} , providing a guideline for constructing the geometries and a wind tunnel for experimental confirmation.

3.2. Wind Tunnel Design

Figure 5 illustrates the wind tunnel design, for which simulations were conducted by varying the diameter of the central cylinder from 50, 55, 60, 65, 70 and 75 cm (Figure 5g). In Figure 8a, a red color represents 12 m/s velocity at the inlet, which is the maximum wind speed to which the wind turbine would be subjected based on the compass rose data for the location of San Juan del Río, Querétaro, Mexico. A diameter of 75 cm was considered for the central cylinder, as the velocities at the wind tunnel walls tend towards 0 m/s, satisfying criterion I established in the methodology.

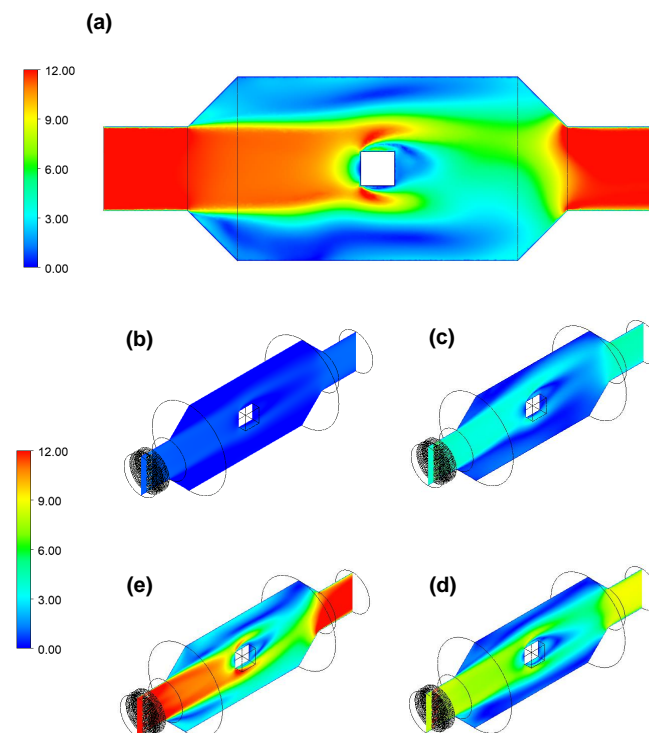


Figure 8. (a) Side view of the velocity contour at 12 m/s. Isometric tunnel view with a longitudinal contour when the airflow director is inserted near the inlet, varying the speed: (b) 1 m/s, (c) 4 m/s, (d) 8 m/s and (e) 12 m/s.

When the airflow director is inserted at the end of the air inlet (Figure 5f), simulation results show an imbalance in the velocity profile. In other words, there is a higher velocity (8.5 m/s) at the top of the wind turbine compared to the bottom (2 m/s), making it not the

optimal choice. If the airflow director is inserted into the central part (Figure 5e), the velocity profile variation for the upper and lower parts of the wind turbine decreases. The best performance is obtained when the airflow director is inserted at the inlet (Figure 5d), as detailed in the simulation behavior in Figure 8b–e. Considering that the air enters at a speed of 1 m/s as shown in Figure 8b, the wind tunnel walls tend towards zero and there is a balance in the upper and lower parts of the control volume where the wind turbine will be located. When the wind speed is increased to 4, 8 and 12 m/s, the behavior is similar, with the best option being to place the airflow director near the inlet. As expected, another effect of the airflow director was the decrease in wind speed, as shown in Figure 8e. When a simulation speed of 12 m/s is set for the inlet, it decreases to 10.5 m/s.

Once it was determined that the wind tunnel cylinder should have a diameter of 100 cm, meeting design criteria I and II, Figure 9 shows the 1:1 scale prototype.

Figure 9 shows the final construction of the wind tunnel, including each of the main components such as the fan, the wind power generation system, the flow director system and the 3D printed rotors that were evaluated in this work.

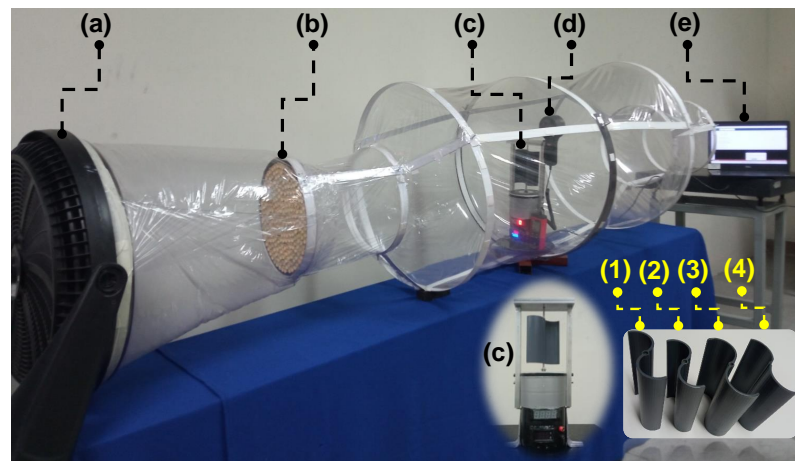


Figure 9. Construction of the wind tunnel and the main components. (a) Fan, (b) flow straighteners, (c) wind turbine, (d) anemometer, (e) laptop and 3D printed rotors: (1) geometry for R_C , (2) geometry for S_{C1} , (3) geometry for S_{C2} and (4) geometry for S_{C3} .

3.3. Characterization of Airflow Fields

Table 3 presents the angular velocity (ω) values for R_C , S_{C1} , S_{C2} and S_{C3} at different wind speeds, which caused the wind turbine to start rotating. Table 3 shows that the R_C requires a wind speed of 2.4 m/s to start rotation, compared to S_{C3} 's best performance of 3.2 m/s. R_C demonstrates superior performance as it operates at lower wind speeds. When using a wind speed standard of 4 m/s for all four rotors, R_C performs best with an angular velocity (ω) of 53.4 rad/s.

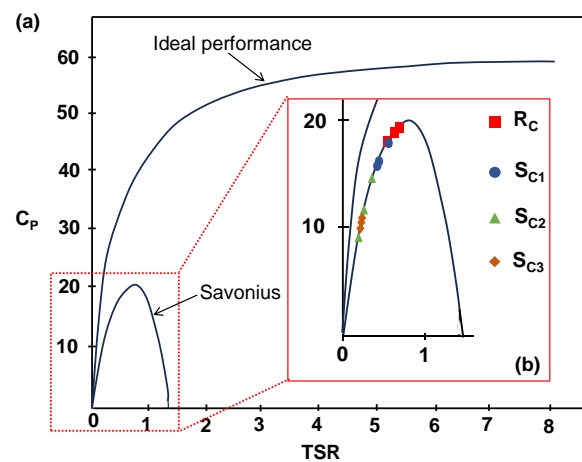
By using Equation (7) to calculate TSR, R_C obtained a value of 0.60, which is the highest, according to Table 3. TSR represents the percentage of wind speed that can be converted into angular velocity in the rotor. This means that the RC can convert up to 60% of the wind speed into angular velocity when operating at a wind speed of 4 m/s.

Figure 10a shows the curve defining the ideal behavior of a wind turbine in terms of TSR versus C_p . The maximum ideal value is 59%. Figure 10a also shows the maximum C_p for an S-type rotor, which has a value of approximately 0.2 (Figure 10a). When relating the TSR values obtained in Table 3 and C_p in Figure 10b, it can be observed that the R_C achieves the highest C_p values, close to approximately 0.19; in decreasing order, it is followed by S_{C1} , S_{C2} and S_{C3} .

For the calculation of the theoretical wind power per swept area, Equation (6) was considered, where the Betz Limit (C_p) is 0.2, the air density (ρ) is 0.9 kg/m³, the wind speed is 5 m/s and the height is 0.12 m. Table 4 displays the results obtained for each case.

Table 3. Results of the experimental characterization of airflow fields.

Rotor	Wind Speed V_w (m/s)	Angular Velocity ω (rad/s)	TSR λ
R_C	2.40	29.53	0.55
	4	53.44	0.60
	5	55.5	0.49
S_{C1}	3.40	29.53	0.39
	4	42.93	0.48
	5	45.03	0.40
S_{C2}	4	29.32	0.26
	4.5	16.96	0.13
	5	33.51	0.23
S_{C3}	3.2	16.96	0.18
	4	24.08	0.21
	5	28.27	0.19

**Figure 10.** Relationship of C_p based on TSR values. (a) A Savonius-type rotor and the ideal case. (b) Close-up with the results for the different calculated TSRs from Table 3.**Table 4.** Calculation of the theoretical power for each case.

Rotor	Rotor Diameter (m)	Power (mW)
R_C	0.09	121.5
S_{C1}	0.09	121.5
S_{C2}	0.07	95.9
S_{C3}	0.07	94.5

Table 4 shows that a larger area in S_{C1} theoretically results in higher power. However, at a wind speed of 2.4 m/s, the R_C achieves a higher angular velocity than in other cases.

3.4. Experimental Moment Behavior

Table 5 displays the results of the moment and angular velocity obtained by directing the air from the fan with the velocities low of 4 m/s, medium of 5 m/s and high of 6 m/s to the rotors in each case, which are anchored to the shaft of the electric generator. The $k\phi$ term determined for the electric generator was 0.001. With the value of $k\phi = 0.001$ according to Equation (8) the torque was calculated for the low velocity (vel_low) and the high velocity (vel_high) as seen in Table 5. P_Low refers to the power calculated with the current value obtained at low fan operating speed and the corresponding moment value according to Table 5 and therefore P_High, the power calculated with the current value and momentum obtained with the fan at high velocity, as Table 5 shows.

According to Table 5, the highest power values are obtained by R_C and S_{C1} . Among these geometries and under the three fan operation options, the R_C achieves the highest power values. On average, these values are 26.6% higher than those of S_{C1} .

Table 5. Angular velocity, moment and power values generated via the three operating speeds of the fan.

Rotor	Angular Velocity ω (rad/s)	Moment μ (Nm)		P_Low (mW)	P_High (mW)
		Vel_LOW	Vel_HIGH		
R_C	53.4			3.47	4.81
	55.5	65	90	6.31	5.00
	59.69			3.88	5.37
S_{C1}	42.93			2.62	3.78
	45.03	61	88	2.75	3.96
	48.17			2.94	4.24
S_{C2}	29.32			1.55	2.17
	33.51	53	74	1.78	2.48
	35.6			1.89	2.63
S_{C3}	24.08			1.30	1.76
	28.27	54	73	1.53	2.06
	32.46			1.75	2.37

MPP Characterization

The graph in Figure 11a displays the power values obtained at different loads used in the electric generator coupled to the R_C . It was found in the initial approach that the MPP is at approximately less than 50 ohms.

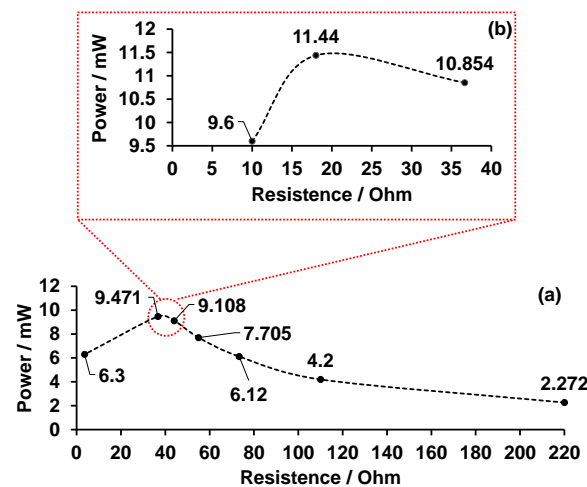


Figure 11. Power vs. Resistance Graph: (a) Low fan operation. (b) High fan operation.

In order to determine the most accurate MPP, resistors with a resistance lower than 50 ohms were tested while the fan speed was set to maximum. The results are presented in Figure 11b, with the MPP being achieved at a resistance value of 18 ohms.

The resistance at the MPP was used to evaluate the cases at maximum fan speed operation. During the first run, the fan was set to maximum speed and the R_C was placed on the rotor shaft for approximately 60 s. This was followed by S_{C1} , S_{C2} and S_{C3} , each for the same time interval, and the maximum values were recorded. Upon analysis of the results, it was observed that S_{C2} and S_{C3} did not achieve the same electrical power values as R_C and S_{C1} . Therefore, they were not evaluated in the second run.

Table 6 presents the results from the two runs and the recorded variables used to calculate power values obtained during the MPP characterization stage. The difference in the maximum values achieved via the R_C is noticeable. When comparing the maxi-

imum values between R_C and S_{C1} , R_C demonstrates a 38% superior performance to S_{C1} . Tables 4, 6 and 7 show that R_C has the highest efficiency at 10.86%.

Table 6. Values of voltage, current and power at the MPP with a resistance of 18 ohms for each evaluated case.

Rotor	Voltage (Volts)	Current (Ampere)	Electrical Power (mW)
R_C	0.52	0.022	11.44
	0.60	0.022	13.2
	0.44	0.018	8.14
S_{C1}	0.50	0.019	9.55
	0.15	0.006	0.9
S_{C3}	0.11	0.005	0.66

Table 7. Efficiency of each rotor using the MPP.

Rotor	Theoretical Power (mW)	Experimental Electrical Power (mW)	Efficiency (%)
R_C	121.5	13.2	10.86
S_{C1}	121.5	9.55	7.86
S_{C2}	95.9	0.90	0.94
S_{C3}	94.5	0.66	0.69

4. Conclusions

A rotor based on the cycloid equation was proposed and its performance was evaluated against three S-type rotors. This was done through numerical simulation using ANSYS® Fluent and experimental characterization using a wind tunnel. The results obtained include the angular velocity, maximum power point, torque and power achieved by each rotor.

The simulation results show that the R_C is 15.0% more efficient than S_{C1} . The RMS power of the simulation overpredicted the theoretical analysis by a factor of 2.78.

The R_C achieved higher TSR values compared to the other rotors, making it a reliable indicator of their performance.

The experimental results indicate that the proposed R_C achieves an electrical power value 38% higher than that of the rotor S_{C1} . The experimental results demonstrate that a rotor based on the cycloid equation achieves an efficiency of 10.86%, while the analyzed S_{C1} only reached 7.86%.

5. Patents

There is a mini-patent in process by the Mexican Institute of Industrial Property with expedient number MX/u/2024/000020.

Author Contributions: Conceptualization, J.E.E.G.-D.; Methodology, J.E.E.G.-D. and M.A.L.-V.; Software, J.E.E.G.-D., J.M.O.-R. and J.M.G.-G.; Investigation, J.E.E.G.-D.; Data curation, J.M.O.-R.; Writing—original draft, J.E.E.G.-D., J.M.O.-R. and J.R.-R.; Writing—review & editing, J.E.E.G.-D., J.M.O.-R., J.R.-R., J.E.S.-O. and M.A.L.-V.; Resources, J.M.G.-G. and J.R.-R.; Project administration, J.M.O.-R., J.R.-R. and J.M.G.-G. All authors have read and agreed to the published version of the manuscript.

Funding: This research did not receive any specific grant from funding agencies in the public, commercial or not-for-profit sectors.

Institutional Review Board Statement: Not applicable.

Informed Consent Statement: Not applicable.

Data Availability Statement: The data is available upon request.

Acknowledgments: The authors of this work would like to acknowledge Juio Ortega-Alejos, Francisco Javier Cruz Pérez, Alicia Arroyo Sanchez, and Abraham Olivares Arroyo for the experimental guidance. The authors also acknowledge the support from the National Council of Humanities Sciences and Technologies.

Conflicts of Interest: The authors declared no potential conflicts of interest concerning the research, authorship and/or publication of this article.

Abbreviations

The following abbreviations are used in this manuscript:

AoA	Angle of Attack
AR	Aspect Ratio
CAD	Computer-Aided Design
CFD	Computational Fluid Dynamics
D	Rotor diameter
DES	Detached Eddy Simulation
DOF	Degree of Freedom
D-VAWT	Darrieus-type Vertical-Axis Wind Turbine
FFT	Fast Fourier Transform
GF	Gurney Flap
HDPE	High Density Poly Ethylene
UHMW	Ultra High Molecular Weight Poly Ethylene
HDWT	H-Darrieus Vertical-Axis Wind Turbine
MPP	Maximum Power Point
P _{High}	Power calculated with the current value and momentum obtained with a velocity high
P _{Low}	Power calculated with the current value and momentum obtained with a velocity low
RMS	Root Mean Square
R_C	Cycloid-type rotor
RCC	Ratio of the airfoil Chord length to the rotor Circumference
RV	Rotate Vector
S_{C1}	S-type rotor to case I
S_{C2}	S-type rotor to case II
S_{C3}	S-type rotor to case III
SB-VAWTs	Straight Blade Vertical Axe Wind Turbine
TSR	Tip Speed Ratio
UDF	User-Defined Function
URANS	Unsteady Reynolds-Averaged-Navier-Stokes
VAWT	Vertical-Axis Wind Turbine
vel _{low}	velocity high
vel _{low}	velocity low
C_p	Power Coefficient
I	Current (A)
J_z	Moment of Inertia (kgm^2)
$k\phi$	Factor experimentally determined
λ	The blade tip speed ratio
θ	Angle (Rad)
P	Power (W)
R	Rotor radius (m)
r	The radius of the generating circle (m)
ρ	Density (kg/m^3)
σ	Solidity
T	Torque o momentum (Nm)
v	Velocity (m/s)
V_w	Wind speed (m/s)
ω	Angular velocity (rad/s)
x	Coordinate on the abscissa axis
y	Coordinate on the ordinate axis

References

1. Ando, Y.; Oku, T.; Yasuda, M.; Ushijima, K.; Murozono, M. A Transportable Photovoltaic Power Generation System Utilizing a SiC Inverter and Spherical Si Solar Cells. *Technologies* **2017**, *5*, 18. [[CrossRef](#)]
2. Hidalgo, H.; Vázquez, N.; Orosco, R.; Huerta-Ávila, H.; Pinto, S.; Estrada, L. Floating Interleaved Boost Converter with Zero-Ripple Input Current Using Variable Inductor. *Technologies* **2023**, *11*, 21. [[CrossRef](#)]
3. Sumaiya, S.; Kardel, K.; El-Shahat, A. Organic Solar Cell by Inkjet Printing—An Overview. *Technologies* **2017**, *5*, 53. [[CrossRef](#)]
4. Kovtunenکو, V.A. The Holby–Morgan Model of Platinum Catalyst Degradation in PEM Fuel Cells: Range of Feasible Parameters Achieved Using Voltage Cycling. *Technologies* **2023**, *11*, 184. [[CrossRef](#)]
5. Kovtunenکو, V.A.; Karpenko-Jereb, L. Lifetime of Catalyst under Voltage Cycling in Polymer Electrolyte Fuel Cell Due to Platinum Oxidation and Dissolution. *Technologies* **2021**, *9*, 80. [[CrossRef](#)]
6. Dorrego-Portela, J.R.; Ponce-Martínez, A.E.; Pérez-Chaltell, E.; Peña-Antonio, J.; Mateos-Mendoza, C.A.; Robles-Ocampo, J.B.; Sevilla-Camacho, P.Y.; Aviles, M.; Rodríguez-Reséndiz, J. Angle Calculus-Based Thrust Force Determination on the Blades of a 10 kW Wind Turbine. *Technologies* **2024**, *12*, 22. [[CrossRef](#)]
7. Day, H.; Ingham, D.; Ma, L.; Pourkashanian, M. Adjoint based optimisation for efficient VAWT blade aerodynamics using CFD. *J. Wind Eng. Ind. Aerodyn.* **2021**, *208*, 104431. [[CrossRef](#)]
8. Zhang, T.; Wang, Z.; Huang, W.; Ingham, D.; Ma, L.; Pourkashanian, M. A numerical study on choosing the best configuration of the blade for vertical axis wind turbines. *J. Wind Eng. Ind. Aerodyn.* **2020**, *201*, 104162. [[CrossRef](#)]
9. Ye, M.; Chen, H.C.; Koop, A. Verification and validation of CFD simulations of the NTNU BT1 wind turbine. *J. Wind Eng. Ind. Aerodyn.* **2023**, *234*, 105336. [[CrossRef](#)]
10. Celik, Y.; Ma, L.; Ingham, D.; Pourkashanian, M. Aerodynamic investigation of the start-up process of H-type vertical axis wind turbines using CFD. *J. Wind Eng. Ind. Aerodyn.* **2020**, *204*, 104252. [[CrossRef](#)]
11. Ghareghani, M.S.M.; Abdolahifar, A.; Karimian, S.M.H. Numerical investigation on the helix angle to smoothen aerodynamic torque output of the 3-PB Darrieus vertical axis wind turbine. *J. Wind Eng. Ind. Aerodyn.* **2023**, *234*, 105323. [[CrossRef](#)]
12. Li, G.; Xu, W.; Li, Y.; Wang, F. Univariate analysis of scaling effects on the aerodynamics of vertical axis wind turbines based on high-resolution numerical simulations: The Reynolds number effects. *J. Wind Eng. Ind. Aerodyn.* **2022**, *223*, 104938. [[CrossRef](#)]
13. Ali, U.; Modrek, M.; Islam, M.; Janajreh, I. Numerical Study of Airfoil Shape and Blade Pitching on Vertical Axis Wind Turbine Through CFD Simulations. In Proceedings of the ASME International Mechanical Engineering Congress and Exposition, Online, 16–19 November 2020; Volume 8. [[CrossRef](#)]
14. Jiang, Y.; Zhao, P.; Zou, L.; Zong, Z.; Wang, K. Two-Dimensional Computational Fluid Dynamics Study on the Performance of Twin Vertical Axis Wind Turbine With Deflector. *J. Energy Resour. Technol.* **2020**, *142*, 081303. [[CrossRef](#)]
15. Ghoneam, S.; Hamada, A.; Sherif, T. Modeling and Optimization for the Dynamic Performance of Vertical-Axis Wind Turbine Composite Blades. *J. Sol. Energy Eng.* **2020**, *143*, 021005. [[CrossRef](#)]
16. Wilberforce, T.; Alaswad, A. Performance analysis of a vertical axis wind turbine using computational fluid dynamics. *Energy* **2023**, *263*, 125892. [[CrossRef](#)]
17. Singh, E.; Roy, S.; Yam, K.S.; Law, M.C. Numerical analysis of H-Darrieus vertical axis wind turbines with varying aspect ratios for exhaust energy extractions. *Energy* **2023**, *277*, 127739. [[CrossRef](#)]
18. Huang, H.; Luo, J.; Li, G. Study on the optimal design of vertical axis wind turbine with novel variable solidity type for self-starting capability and aerodynamic performance. *Energy* **2023**, *271*, 127031. [[CrossRef](#)]
19. Farzadi, R.; Bazargan, M. 3D numerical simulation of the Darrieus vertical axis wind turbine with J-type and straight blades under various operating conditions including self-starting mode. *Energy* **2023**, *278*, 128040. [[CrossRef](#)]
20. Tong, G.; Yang, S.; Li, Y.; Feng, F. Effects of blade tip flow on aerodynamic characteristics of straight-bladed vertical axis wind turbines. *Energy* **2023**, *283*, 129105. [[CrossRef](#)]
21. Li, G.; Li, Y.; Li, J.; Huang, H.; Huang, L. Research on dynamic characteristics of vertical axis wind turbine extended to the outside of buildings. *Energy* **2023**, *272*, 127182. [[CrossRef](#)]
22. Shubham, S.; Naik, K.; Sachar, S.; Ianakiev, A. Performance analysis of low Reynolds number vertical axis wind turbines using low-fidelity and mid-fidelity methods and wind conditions in the city of Nottingham. *Energy* **2023**, *279*, 127904. [[CrossRef](#)]
23. Tong, G.; Li, Y.; Tagawa, K.; Feng, F. Effects of blade airfoil chord length and rotor diameter on aerodynamic performance of straight-bladed vertical axis wind turbines by numerical simulation. *Energy* **2023**, *265*, 126325. [[CrossRef](#)]
24. Xu, W.; Li, C.-C.; Huang, S.-X.; Wang, Y. Aerodynamic performance improvement analysis of Savonius Vertical Axis Wind Turbine utilizing plasma excitation flow control. *Energy* **2022**, *239*, 122133. [[CrossRef](#)]
25. Hohman, T.C.; Martinelli, L.; Smits, A.J. The effect of blade geometry on the structure of vertical axis wind turbine wakes. *J. Wind Eng. Ind. Aerodyn.* **2020**, *207*, 104328. [[CrossRef](#)]
26. Kuang, L.; Zhang, R.; Su, J.; Shao, Y.; Zhang, K.; Chen, Y.; Zhang, Z.; Tu, Y.; Zhou, D.; Han, Z.; et al. Systematic investigation of effect of rotor solidity on vertical-axis wind turbines: Power performance and aerodynamics analysis. *J. Wind Eng. Ind. Aerodyn.* **2023**, *233*, 105284. [[CrossRef](#)]
27. Vergaerde, A.; Troyer, T.D.; Muggiasca, S.; Bayati, I.; Belloli, M.; Kluczevska-Bordier, J.; Parneix, N.; Silvert, F.; Runacres, M.C. Experimental characterisation of the wake behind paired vertical-axis wind turbines. *J. Wind Eng. Ind. Aerodyn.* **2020**, *206*, 104353. [[CrossRef](#)]

28. Thomai, M.P.; Sivamani, S.; Venkatesan, H. Experimental and Numerical Investigation to Assess the Performance of Helical Bach Vertical Axis Wind Turbine at Low Wind Velocity Conditions. *J. Sol. Energy Eng.* **2022**, *144*, 051010. [[CrossRef](#)]
29. Yan, Y.; Avital, E.; Williams, J.; Cui, J. Aerodynamic performance improvements of a vertical axis wind turbine by leading-edge protuberance. *J. Wind Eng. Ind. Aerodyn.* **2021**, *211*, 104535. [[CrossRef](#)]
30. Kim, D.; Gharib, M. Efficiency improvement of straight-bladed vertical-axis wind turbines with an upstream deflector. *J. Wind Eng. Ind. Aerodyn.* **2013**, *115*, 48–52. [[CrossRef](#)]
31. Thomai, M.P.; Thangaraj, M.; Palanivel, S.; Sivamani, S. Numerical Simulation of Cluster of Small Vertical Axis Wind Turbine to Develop a Wind Tree for Low Wind Speed Regime. In Proceedings of the Gas Turbine India Conference, Bangalore, India, 7–8 December 2017; Volume 2. [[CrossRef](#)]
32. Zheng, H.D.; Zheng, X.Y.; Lei, Y. Model Test of a Novel Floating Vertical-Axis Wind Turbine Under Wind and Wave Joint Loads. In Proceedings of the International Conference on Offshore Mechanics and Arctic Engineering, Online, 21–30 June 2021; Volume 9. [[CrossRef](#)]
33. Shah, O.R.; Jamal, M.A.; Khan, T.I.; Qazi, U.W. Experimental and Numerical Evaluation of Performance of a Variable Pitch Vertical-Axis Wind Turbine. *J. Energy Resour. Technol.* **2021**, *144*, 061303. [[CrossRef](#)]
34. Ghoneam, S.M.; Hamada, A.A.; Sherif, T.S. Dynamic Analysis of the Optimized Savonius Vertical Axis Wind Turbine Composite Blades. *J. Sol. Energy Eng.* **2021**, *143*, 054502. [[CrossRef](#)]
35. Su, J.; Chen, Y.; Zhou, D.; Han, Z.; Bao, Y. Swept Blade for Performance Improvement on a Vertical Axis Wind Turbine. In Proceedings of the International Conference on Offshore Mechanics and Arctic Engineering, Online, 3–7 August 2020; Volume 9. [[CrossRef](#)]
36. Roy, S.; Branger, H.; Luneau, C.; Bourras, D.; Paillard, B. Design of an Offshore Three-Bladed Vertical Axis Wind Turbine for Wind Tunnel Experiments. In Proceedings of the International Conference on Offshore Mechanics and Arctic Engineering, Trondheim, Norway, 25–30 June 2017; Volume 10. [[CrossRef](#)]
37. Seralathan, S.; Thomai, M.P.; Jayakumar, R.L.; Reddy, B.V.L.; Venkatesan, H. Experimental and Numerical Assessment of Cross Flow Vertical Axis Wind Turbine. In Proceedings of the Gas Turbine India Conference, Chennai, India, 5–6 December 2019; Volume 2. [[CrossRef](#)]
38. Su, H.; Meng, H.; Guo, J.; Qu, T.; Lei, L. Wind Tunnel Experiment on the Aerodynamic Interaction Between Vertical Axis Wind Turbine Pair. In Proceedings of the Fluids Engineering Division Summer Meeting, Online, 10–12 August 2021; Volume 2. [[CrossRef](#)]
39. Tanzawa, Y.; Sato, T.; Hashizume, T. Wind Direction Characteristics of a Vertical Axis Wind Turbine Using the Mechanism of a Bird's Wing With a Wind Collector. In Proceedings of the ASME Power Conference, Denver, CO, USA, 12–14 July 2011; Volume 2, pp. 557–561. [[CrossRef](#)]
40. Rahman, M.; Salyers, T.; Ahmed, M.; ElShahat, A.; Soloiu, V.; Maroha, E. Investigation of Aerodynamic Performance of Helical Shape Vertical-Axis Wind Turbine Models With Various Number of Blades Using Wind Tunnel Testing and Computational Fluid Dynamics. In Proceedings of the ASME International Mechanical Engineering Congress and Exposition, Phoenix, AZ, USA, 11–17 November 2016; Volume 7. [[CrossRef](#)]
41. Naik, K.; Sahoo, N. Synergistic Effect of J-Shape Airfoil on the Performance of Darrieus-Type Straight-Bladed Vertical Axis Wind Turbine. *J. Energy Resour. Technol.* **2023**, *145*, 101301. [[CrossRef](#)]
42. Sarkar, D.; Shukla, S.; Alom, N.; Sharma, P.; Bora, B.J. Investigation of a Newly Developed Slotted Bladed Darrieus Vertical Axis Wind Turbine: A Numerical and Response Surface Methodology Analysis. *J. Energy Resour. Technol.* **2022**, *145*, 051302. [[CrossRef](#)]
43. Zilberman, M.; Sbaih, A.A.; Hadad, I. Optimized Small Vertical Axis Wind Turbine (VAWT), Phase I. In Proceedings of the Gas Turbine India Conference. American Society of Mechanical Engineers, Online, 2–3 December 2021. [[CrossRef](#)]
44. Kumar, K.K.S.; Kulkarni, V.; Sahoo, N. Investigation on Flow Characteristics and Performance of a Vertical Axis Wind Turbine with Deflector Plates. In Proceedings of the Gas Turbine India Conference, Chennai, India, 5–6 December 2019; Volume 2. [[CrossRef](#)]
45. Liu, X.; Chen, Q.; Yang, B.; Song, M. Research on the Performance of a Vertical-Axis Wind Turbine With Helical Blades by Detached Eddy Simulation. *J. Sol. Energy Eng.* **2020**, *142*, 031008. [[CrossRef](#)]
46. Mohammed, A.A.; Sahin, A.Z.; Ouakad, H.M. Numerical Investigation of a Vertical Axis Wind Turbine Performance Characterization Using New Variable Pitch Control Scheme. *J. Energy Resour. Technol.* **2019**, *142*, 031302. [[CrossRef](#)]
47. Yan, Y.; Avital, E.; Williams, J.; Cui, J. Performance Improvements for a Vertical Axis Wind Turbine by Means of Gurney Flap. *J. Fluids Eng.* **2019**, *142*, 021205. [[CrossRef](#)]
48. Li, Q.; Cai, C.; Maeda, T.; Kamada, Y.; Shimizu, K.; Dong, Y.; Zhang, F.; Xu, J. Visualization of aerodynamic forces and flow field on a straight-bladed vertical axis wind turbine by wind tunnel experiments and panel method. *Energy* **2021**, *225*, 120274. [[CrossRef](#)]
49. Hosseini, A.; Goudarzi, N. CFD and Control Analysis of a Smart Hybrid Vertical Axis Wind Turbine. In Proceedings of the ASME Power Conference, Lake Buena Vista, FL, USA, 24–28 June 2018; Volume 1. [[CrossRef](#)]
50. Korprasertsak, N.; Leephakpreeda, T. Analysis and optimal design of wind boosters for Vertical Axis Wind Turbines at low wind speed. *J. Wind Eng. Ind. Aerodyn.* **2016**, *159*, 9–18. [[CrossRef](#)]

51. Vlasveld, E.; Huijs, F.; Savenije, F.; Paillard, B. Coupled Dynamics of a Vertical Axis Wind Turbine (VAWT) With Active Blade Pitch Control on a Semi-Submersible Floater. In Proceedings of the International Conference on Offshore Mechanics and Arctic Engineering, Madrid, Spain, 17–22 June 2018; Volume 10. [\[CrossRef\]](#)
52. Mishra, N.; Gupta, A.S.; Dawar, J.; Kumar, A.; Mitra, S. Numerical and Experimental Study on Performance Enhancement of Darrieus Vertical Axis Wind Turbine With Wingtip Devices. *J. Energy Resour. Technol.* **2018**, *140*, 121201. [\[CrossRef\]](#)
53. Wang, Z.; Zhuang, M. A Numerical Study on the Performance Improvement for a Vertical-Axis Wind Turbine at Low Tip-Speed-Ratios. In Proceedings of the Fluids Engineering Division Summer Meeting, Waikoloa, HI, USA, 30 July–3 August 2017; Volume 1A. [\[CrossRef\]](#)
54. Chen, Y.; Guo, P.; Zhang, D.; Chai, K.; Zhao, C.; Li, J. Power improvement of a cluster of three Savonius wind turbines using the variable-speed control method. *Renew. Energy* **2022**, *193*, 832–842. [\[CrossRef\]](#)
55. Nag, A.K.; Sarkar, S. Performance analysis of Helical Savonius Hydrokinetic turbines arranged in array. *Ocean Eng.* **2021**, *241*, 110020. [\[CrossRef\]](#)
56. Dion, J.L.; Pawelski, Z.; Chianca, V.; Zdziennicki, Z.; Peyret, N.; Uszpolewicz, G.; Ormezowski, J.; Mitukiewicz, G.; Lelasseux, X. Theoretical and Experimental Study for An Improved Cycloid Drive Model. *J. Appl. Mech.* **2019**, *87*, 011002. [\[CrossRef\]](#)
57. Li, X.; Li, C.; Wang, Y.; Chen, B.; Lim, T.C. Analysis of a Cycloid Speed Reducer Considering Tooth Profile Modification and Clearance-Fit Output Mechanism. *J. Mech. Des.* **2017**, *139*, 033303. [\[CrossRef\]](#)
58. Zhu, C.; Sun, Z.; Liu, H.; Song, C.; Li, Z.; Wang, Z. Effect of the Shape of Inlet Oil-Supply Layer on Starved Lubrication Performance of a Cycloid Drive. In Proceedings of the International Design Engineering Technical Conferences and Computers and Information in Engineering Conference, Boston, MA, USA, 2–5 August 2015; Volume 10. [\[CrossRef\]](#)
59. Sensinger, J.W. Efficiency of High-Sensitivity Gear Trains, Such as Cycloid Drives. *J. Mech. Des.* **2013**, *135*, 071006. [\[CrossRef\]](#)
60. Rashidi, Y.; Arzanpour, S.; Tabatabaian, M. Energy Absorption and Dissipation Performance in Cycloid Guided Pendulum Absorbers. In Proceedings of the ASME International Mechanical Engineering Congress and Exposition, Vancouver, BC, Canada, 12–18 November 2010; Volume 13, pp. 297–302 [\[CrossRef\]](#)
61. Choi, T.H.; Kim, M.S.; Lee, G.S.; Jung, S.Y.; Bae, J.H.; Kim, C. Design of Rotor for Internal Gear Pump Using Cycloid and Circular-Arc Curves. *J. Mech. Des.* **2012**, *134*, 011005. [\[CrossRef\]](#)
62. Kim, K.-H.; Lee, C.-S.; Ahn, H.J. Torsional Rigidity of a Cycloid Drive Considering Finite Bearing and Hertz Contact Stiffness. In Proceedings of the International Design Engineering Technical Conferences and Computers and Information in Engineering Conference, San Diego, CA, USA, 30 August–2 September 2009; Volume 6, pp. 125–130. [\[CrossRef\]](#)
63. Sensinger, J.W. Unified Approach to Cycloid Drive Profile, Stress, and Efficiency Optimization. *J. Mech. Des.* **2010**, *132*, 024503. [\[CrossRef\]](#)
64. Xu, W.; Fu, Y.; Du, R. A Power Flow Analysis and Control Methodology for Cycloid Gear Train in Precision Transmission. In Proceedings of the International Conference on Integration and Commercialization of Micro and Nanosystems, Sanya, China, 10–13 January 2007; pp. 41–46. [\[CrossRef\]](#)
65. Tutulan, F.G.; Nagamura, K.; Ikejo, K. Tooth Root Stress and Tooth Contact Stress of the Modified Cycloid Helical Gear. In Proceedings of the International Design Engineering Technical Conferences and Computers and Information in Engineering Conference, Chicago, IL, USA, 2–6 September 2003; Volume 4, pp. 91–96. [\[CrossRef\]](#)
66. Zhou, J. A New Cycloid Drive With Ceramic Balls as Its Gear Teeth. In Proceedings of the International Design Engineering Technical Conferences and Computers and Information in Engineering Conference, Long Beach, CA, USA, 24–28 September 2005; Volume 5b, pp. 891–895. [\[CrossRef\]](#)
67. Li, X.; He, W.; Li, L.; Schmidt, L.C. A New Cycloid Drive With High-Load Capacity and High Efficiency. *J. Mech. Des.* **2004**, *126*, 683–686. [\[CrossRef\]](#)
68. Blanche, J.G.; Yang, D.C.H. Cycloid Drives With Machining Tolerances. *J. Mech. Transm. Autom. Des.* **1989**, *111*, 337–344. [\[CrossRef\]](#)
69. Pollitt, E.P. Some Applications of the Cycloid in Machine Design. *J. Eng. Ind.* **1960**, *82*, 407–414. [\[CrossRef\]](#)
70. Mao, H.; Liu, G.; Zeng, D.; Cao, Y.; He, K.; Du, R. A New Design of Cycloidal Planetary Reducer With Internal Cycloidal Profile. In Proceedings of the ASME International Mechanical Engineering Congress and Exposition ASME International Mechanical Engineering Congress and Exposition, Pittsburgh, PA, USA, 9–15 November 2018; Volume 2. [\[CrossRef\]](#)
71. Ohya, Y.; Karasudani, T.; Sakurai, A.; Abe, K.-I.; Inoue, M. Development of a shrouded wind turbine with a flanged diffuser. *J. Wind Eng. Ind. Aerodyn.* **2008**, *96*, 524–539. [\[CrossRef\]](#)
72. Liu, J.; Song, M.; Chen, K.; Wu, B.; Zhang, X. An optimization methodology for wind lens profile using Computational Fluid Dynamics simulation. *Energy* **2016**, *109*, 602–611. [\[CrossRef\]](#)
73. Zimmer, F.; Gagnon, L. Study on the Performance of a Cycloidal Rotor in Hover at Different Reynolds Numbers. *J. Fluids Eng.* **2023**, *145*, 051204. [\[CrossRef\]](#)
74. Ben-Abu, Y.; Wolfson, I.; Wolfson, I.; Wolfson, I. Energy, Christiaan Huygens, and the Wonderful Cycloid—Theory versus Experiment. *Symmetry* **2018**, *10*, 111. [\[CrossRef\]](#)
75. Sobczak, K. Numerical investigations of an influence of the aspect ratio on the Savonius rotor performance. *J. Phys. Conf. Ser.* **2018**, *1101*, 012034. [\[CrossRef\]](#)
76. Mohamed, M.; Janiga, G.; Pap, E.; Thévenin, D. Optimal blade shape of a modified Savonius turbine using an obstacle shielding the returning blade. *Energy Convers. Manag.* **2011**, *52*, 236–242. [\[CrossRef\]](#)

77. Sobczak, K.; Obidowski, D.; Reorowicz, P.; Marchewka, E. Numerical Investigations of the Savonius Turbine with Deformable Blades. *Energies* **2020**, *13*, 3717. [[CrossRef](#)]
78. Aramendia, I.; Fernandez-Gamiz, U.; Zulueta, E.; Saenz-Aguirre, A.; Teso-Fz-Betoño, D. Parametric Study of a Gurney Flap Implementation in a DU91W(2)250 Airfoil. *Energies* **2019**, *12*, 294. [[CrossRef](#)]
79. Kacprzak, K.; Sobczak, K. Numerical analysis of the flow around the Bach-type Savonius wind turbine. *J. Phys. Conf. Ser.* **2014**, *530*, 012063. [[CrossRef](#)]
80. Sakri, F.M.; Ali, M.S.M.; Salim, S.A.Z.S. Computational investigations and grid refinement study of 3D transient flow in a cylindrical tank using OpenFOAM. *IOP Conf. Ser. Mater. Sci. Eng.* **2016**, *152*, 012058. [[CrossRef](#)]
81. Procedure for Estimation and Reporting of Uncertainty Due to Discretization in CFD Applications. *J. Fluids Eng.* **2008**, *130*, 078001. [[CrossRef](#)]
82. METEOCAST Incorporation. Available online: <https://meteocast.net/forecast/mx/san-juan-del-rio/> (accessed on 1 November 2023).

Disclaimer/Publisher’s Note: The statements, opinions and data contained in all publications are solely those of the individual author(s) and contributor(s) and not of MDPI and/or the editor(s). MDPI and/or the editor(s) disclaim responsibility for any injury to people or property resulting from any ideas, methods, instructions or products referred to in the content.